Mapping the biological activities of filamentous oxygenic photogranules

Hicham Ouazaite, Kim Milferstedt, Jérôme Hamelin, Elie Desmond-Le Quéméner

▶ **To cite this version:**

Hicham Ouazaite, Kim Milferstedt, Jérôme Hamelin, Elie Desmond-Le Quéméner. Mapping the biological activities of filamentous oxygenic photogranules. Biotechnology and Bioengineering, 2021, 118 (2), pp.601-611. 10.1002/bit.27585 . hal-02981499

HAL Id: hal-02981499
https://hal.inrae.fr/hal-02981499v1

Submitted on 29 Jul 2024

HAL is a multi-disciplinary open access archive for the deposit and dissemination of scientific research documents, whether they are published or not. The documents may come from teaching and research institutions in France or abroad, or from public or private research centers.

L'archive ouverte pluridisciplinaire **HAL**, est destinée au dépôt et à la diffusion de documents scientifiques de niveau recherche, publiés ou non, émanant des établissements d'enseignement et de recherche français ou étrangers, des laboratoires publics ou privés.

Mapping the biological activities of filamentous oxygenic photogranules

Hicham Ouazaite, Kim Milferstedt, Jérôme Hamelin, Elie Desmond-Le Quéméner*

INRAE, Univ Montpellier, LBE, 102 Avenue des Etangs, 11100 Narbonne, France
*corresponding author: elie.lequemener@inrae.fr

Abstract

Oxygenic photogranules have been suggested as alternatives to activated sludge in wastewater treatment. Challenging for modelling photogranule-based processes is the heterogeneity of photogranule morphologies, resulting in different activities by photogranule type. The measurement of microscale-activities of filamentous photogranules is particularly difficult because of their labile interfaces. We present here an experimental and modeling approach to quantify phototrophic O_2 production, heterotrophic O_2 consumption and O_2 diffusion in filamentous photogranules. We used planar optodes for the acquisition of spatio-temporal oxygen distributions combined with 2D mathematical modelling. Light penetration into the photogranule was the factor controlling photogranule activities. The spatial distribution of heterotrophs and phototrophs had less impact. The photosynthetic response of filaments to light was detectable within seconds, emphasizing the need to analyze dynamics of light exposure of individual photogranules in photobioreactors. Studying other recurring photogranule morphologies will eventually enable the description of photogranule-based processes as the interplay of interacting photogranule populations.

Keywords

wastewater treatment, syntrophy, modelling, phototrophic biofilms, oxygen gradients

1 Introduction

Recently, oxygenic photogranules (OPGs) have been described as a novel kind of photogranular biofilm (Milferstedt et al., 2017a, 2017b). OPGs are dense bacterial aggregates, typically a few millimeters in diameter, characterized by an outer layer mainly composed of filamentous cyanobacteria. The production of oxygen by these cyanobacteria via photosynthesis is typically coupled with the oxygen consumption of heterotrophic bacteria that convert organic matter, e.g., from wastewater, into CO_2, which is immediately used by cyanobacteria for biomass synthesis. This syntrophic relationship between bacteria makes photogranules a promising candidate biomass for wastewater treatment (Abouhend et al., 2020, 2018). In photogranules, external aeration becomes unnecessary and high biomass yields and rapid settling enable the efficient recovery of resources. External aeration in conventional activated sludge is currently the major energy expenditure of wastewater treatment plants (Longo et al., 2016; Shoener et al., 2014).

This expenditure may be off-set in a bioprocess using OPGs by the energetic requirements of mixing and the potential supply of electric light for pollution removal. Light availability is directly linked to the activity of OPGs. Here, we examine the balance of activity between phototrophs and heterotrophs within the granule with the aim to understand the fundamental functioning of photogranules. This understanding will help optimizing the overall performance at the process scale. We use oxygen fluxes as proxy for activity at the microscopic scale. So far, no details on the biological activity at the micro-scale of an OPG have been reported as current OPG research mostly focusses on deciphering the mechanisms of photogranulation (Abouhend et al., 2020; Ansari et al., 2019; Milferstedt et al., 2017b; Stauch-White et al., 2017) and the potential application of these granules for wastewater treatment (Abouhend et al., 2018; Trebuch et al., 2020).

Within a single laboratory-scale photobioreactor, we have observed the coexistence of a range of different OPG morphologies, from filament-covered OPGs to OPGs resembling nearly perfect spheres. It is likely that the various morphologies influence their respective physiological activities.

Oxygen fluxes within spherical OPGs (**Fig. 1**) can be resolved using conventional microelectrodes of the Clark type (Revsbech and Jørgensen, 1986) or polarographic electrodes (Mancuso et al., 2000). These tools are suitable for biofilms, or more specifically granules, with well resolved, stable interfaces for gradient measurements from the surface to the inside of the sample. From a limited number of measurements, the behavior of a larger surface or volume can often be extrapolated. OPGs with labile, flexible and potentially moving filaments at the surface (**Fig. 1**) do not have a stable granule-bulk interface. Their biological activity is greatly influenced by external flow and the boundary conditions. The use of micro-electrodes and the interpretation of their results is challenging as sufficient data reflecting this heterogeneity cannot be easily recorded. This type of filamentous morphologies requires the development of dedicated approaches.

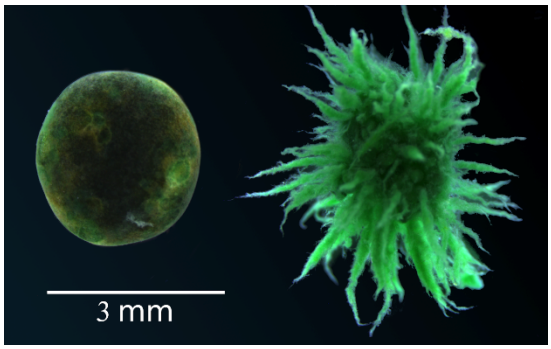

Fig. 1: Different photogranule morphologies as observed in one photobioreactor: left a sphere-like morphology; right a filamentous morphology.

Planar optodes are a promising technology to investigate the spatio-temporal distributions of O_2 in microbial assemblages (Glud et al., 2001; Rubol et al., 2018; Wenzhöfer and Glud, 2004), sediments and soils (Koop-Jakobsen et al., 2018; Pischedda et al., 2008), and possibly filamentous photogranules. The optode technology uses the luminescence of oxygen sensitive indicators immobilized in a hydrophobic polymeric matrix. The measurement is based on the indicator dye quenched by the molecule of interest. The emitted light is then recorded by a ratiometric camera (Larsen et al., 2011; Quaranta et al., 2012). Here we examine the suitability of planar optodes for measuring oxygen dynamics for filamentous photogranules. We developed a simple 2D reaction-diffusion model using only two parameters (maximum oxygen production rate (q_{p0}) and maximum respiration rate (q_{r0})) to decipher the relative contributions of respiration, photosynthesis and diffusion based on oxygen concentrations derived from optode images. This important differentiation is not accessible from the oxygen distributions alone. We show how our coupled approach provides essential data on the activity and properties of the filaments of a photogranule.

2 Materials and Methods

2.1 Bioreactor operation and photogranule sampling

A 4-L sequencing batch photobioreactor was operated with 6-hours cycles under constant illumination of 100 $\mu mol \cdot m^{-2} \cdot s^{-1}$ of photosynthetic active radiation (PAR) at the reactor surface. The feed was a synthetic wastewater with a chemical oxygen demand of 120 $mg \cdot L^{-1}$ and the following composition according to Nopens et al (2001): peptone 8.7 $mg \cdot L^{-1}$, yeast extract 26.1 $mg \cdot L^{-1}$, starch

61 mg·L^{-1}, sodium acetate 42.2 mg·L^{-1}, KH_2PO_4 11.7 mg·L^{-1}, $MgHPO_4 \cdot 3\ H_2O$ 14.5 mg·L^{-1}, urea 45.9 mg·L^{-1}, NH_4Cl 34.2 mg·L^{-1}, $FeSO_4 \cdot 7\ H_2O$ 2.9 mg·L^{-1}.

The OPGs in the photobioreactor showed different morphologies, with the coexistence of spherical and filamentous OPGs (**Fig. 1**). One filamentous OPG of the maximum dimensions of 8.5 mm × 4.5 mm was sampled at the end of a SBR cycle, i.e., after 5 hours of the reaction cycle and was immediately used for extensive imaging of oxygen distributions. For the evaluation of the optode technology and the demonstrate the applicability of capturing oxygen dynamics, the in-depth evaluation of one filamentous photogranule is acceptable.

2.2 Dynamics of oxygen distribution

Oxygen imaging was performed with a PreSens VisiSensTM planar optode (Tschiersch et al., 2012) (**Fig. 2**). A piece of about 60 mm^2 oxygen sensitive sensor foil (SF-RPSU4, PreSens) was glued inside a Petri dish using silicone gel (Silicone rubber compound RS 692-542, RS Components Ltd., Corby, UK). The filamentous OPG was then placed on the sensing foil and a microscopy cover slip was carefully placed on it to prevent the photogranule to float, making sure not to flatten or otherwise disturb the photogranule geometry. The experimental set-up allows the measurement of oxygen distributions at the photogranule surface in contact with the sensor foil. Some minor parts of the photogranule periphery could not be placed onto the reactive surface of the sensor foil because of steric reasons. This did not impact the experimental set-up and analysis.

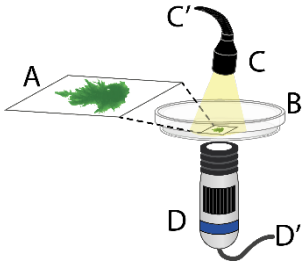

Fig. 2: Schematic display of the experimental set-up to map the oxygen dynamics in a photogranule. (A) filamentous OPG on oxygen sensitive sensor foil in a (B) Petri dish filled with water; (C) goose neck providing light at an intensity of 100 PAR, connected to (C') an external LED light source. Dynamics of oxygen were collected using (D) a camera and recorded on (D') a personal computer.

Then, the Petri dish was filled with air-saturated tap water and closed. The Petri dish was immediately placed on top of the VisiSens camera (Detector Unit DU01, PreSens). The experiment was conducted over 112 minutes during which 130 images of oxygen distributions were recorded over two dark phases (0 – 35 min, 70 – 88 min) and two light phases (35 – 70 min, 88 – 112 min). Each image acquisition consisted of a cycle with a length of 52 s, partitioned in a reaction part (32 s) and an image acquisition part (20 s). Depending on the illumination phase, the reaction part was either in darkness (dark phases) or illuminated with externally provided cold white light at 100 µmol·$m^{-2} \cdot s^{-1}$ of photosynthetically active radiation (PAR) (SCHOTT KL2500LED). The acquisition phase was always in the absence of external light. Corrected for the time of image acquisition, the photogranule received on average 61 PAR during the light phases of the experiment. During image acquisition, the VisiSens system emits 9 µmol·$m^{-2} \cdot s^{-1}$ as PAR at the lens of the camera. This light is required for the excitation of the photosensitive film, even during the dark phases and did not have a measureable effect on photosynthesis of the system.

The VisiSens images were calibrated after their acquisition according to the manufacturer's procedure by recording a single image of the sensor foil and applying a two-point calibration with a

drop of deoxygenated water (tap water stripped with N_2) for 0% O_2 and a drop of water in equilibrium with air for 21% O_2 saturation.

At the end of the experiment, the exact position and geometry of the filamentous OPG on the sensor foil was determined on an image taken with a stereomicroscope (M205FA, Leica Microsystems GmbH, Wetzlar, Germany). The original color image was converted to an 8-bit grey level image.

2.3 Data acquisition and analysis

The time series of oxygen distributions were recorded as PNG images (AnalytiCal 1 Software VA.12, VisiSens). The calibration was performed using the evaluation module of the software following the manufacturer's instructions. The calibrated images were saved in the VisiSens proprietary RAW format and then converted into the ImageJ format "IMJ" (Schneider et al., 2012) using the VisiSens Raw data Interface. Each image has the size of 1280 × 1024 pixels, displaying the oxygen sensitive sensor foil on an area of 925 × 880 pixels. This area corresponds to about 8.3 × 7.5 mm^2. The spatial resolution on the images is 8.9 $\mu m \cdot pixel^{-1}$. The images were then imported as arrays to MATLAB (version R2018b, MathWorks, USA) and dynamics of oxygen concentrations were associated with the morphology of the photogranule.

2.4 Model description, linking oxygen fluxes and microbial activities

A 2D model describing the dynamics of oxygen diffusion with consumption, and production through heterotrophic and phototrophic activities was created to differentiate the impact of each process on the dynamics of measured oxygen concentrations. We used COMSOL Multiphysics (version 5.3a, Comsol Inc., Burlington, USA) for this model. We opted for a 2D model as the three-dimensional (3D) shape of the photogranule was complex and could not be approximated with a simple geometry.

The computational domain (**Fig. 3b**) was extracted from the stereomicroscopic image (**Fig. 3a**) using the MATLAB contour function and then imported to COMSOL Multiphysics using the live link COMSOL-MATLAB interface. The domain was scaled to the size of the oxygen images (8.3 × 7.5 mm^2). The Petri dish wall was used as boundary condition without mass flow and an O_2 flux set to zero. A triangular mesh was applied on the whole image, with a finest meshing at the vicinity of the photogranule contour. The maximum resolution of 8.9 $\mu m \cdot pixel^{-1}$ for the recorded oxygen images was used for the finest meshing (**Fig. 3c**). At this resolution, numerical problems caused by derived unbalanced forces could be avoided. This resolution was not applied on the whole image to avoid prohibitive computing times.

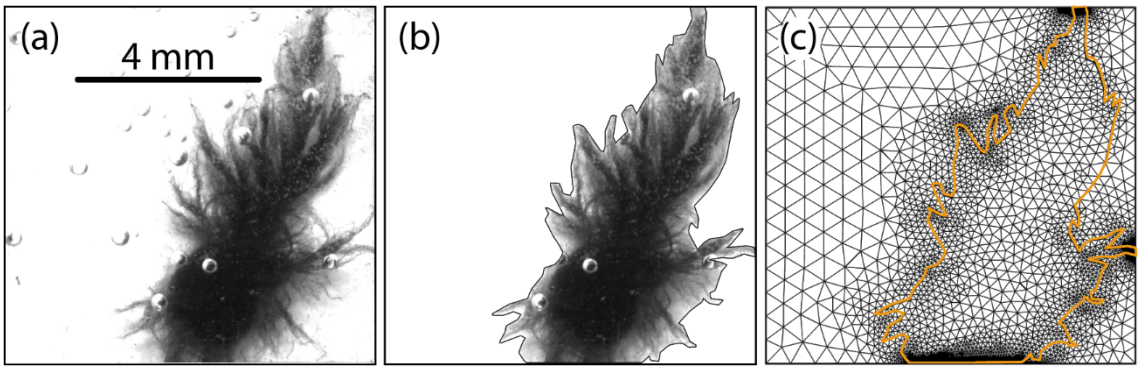

Fig. 3: OPG image and its processing for computation of the geometry: (a) stereomicroscopic image for determination of biomass density based on grey levels; (b) OPG contour calculated based on (a); (c) domain mesh for modelling, with smaller mesh size where oxygen dynamics were higher, e.g. the bulk-photogranule interface, or where for numerical convergence a higher density of points was required, e.g., at the boundaries.

2.5 Assumptions for the mathematical model

Growth of bacteria was neglected since the experimental duration of 112 min was short compared to the assumed growth rates of microorganisms in photogranules. During the experiment the availability of organic matter for heterotrophic respiration and HCO_3^- for photosynthesis remained constant. HCO_3^- was present in excess for photosynthesis due to the hardness of the local tap water of 4.0 ± 0.2 mM as HCO_3^- (https://orobnat.sante.gouv.fr/orobnat/rechercherResultatQualite.do). This concentration was considered not rate-limiting for photosynthesis as the K_S for HCO_3^- of 0.1 mM HCO_3^- (Wolf et al., 2007) is well above the natural availability of HCO_3^-. Thus, dissolved O_2 was the only chemical species considered in this analysis.

The dynamic diffusion-reaction (**Eq. 1**) for dissolved O_2 is:

$$\frac{\partial c}{\partial t} - \nabla \cdot (D \cdot \nabla \mathrm{c}) = r$$

Eq. 1

where *c* is the dissolved oxygen concentration, *D* the diffusion coefficient for oxygen and *r* the net oxygen reaction rate. The diffusion coefficient for oxygen (*D*) is taken as constant throughout the photogranule and equals the diffusion coefficient in water at 20 °C (Wolf et al., 2007). Therefore, *D* equals $2.01 \cdot 10^{-9}$ $m^2 \cdot s^{-1}$ as for dilute solutions. The net O_2 reaction rate (*r*) is zero outside the granule, while being computed from photosynthesis (r_p) and heterotrophic respiration rates within the photogranule (r_r) (**Eq. 2**):

$$r = r_p - r_r$$

Eq. 2

The rate of oxygen production by phototrophs was considered linearly proportional to light intensity and could be approximated to first order kinetics (**Eq. 3**), since the experiments were performed under light-limiting conditions for filamentous cyanobacteria (Staal et al., 2002) (Faizi and Steuer, 2019). The rate of oxygen consumption was modeled using a Monod equation (**Eq. 4**).

$$r_r = q_r(f) \cdot \frac{C}{C + K}$$

Eq. 3

$$r_p = q_p(f) \cdot I(f)$$

Eq. 4

where $q_r(f)$ is the maximal respiration rate, *C* the dissolved O_2 concentration, *K* the half saturation constant with a value of 0.5 $mg \cdot L^{-1}$ (Horn and Hempel, 1997), $q_p(f)$ the maximal photosynthesis rate and *I(f)* the light intensity. The variable *f* was introduced to account for an assumed local biomass density. For this, grey levels in Erreur ! Source du renvoi introuvable.**g** were converted to a variable *f* comprised between 0 (white) and 1 (black) (Erreur ! Source du renvoi introuvable.**f**) which was used as a proxy for surface-based biomass density. The use of the function *f* is introduced in the Results section below (**Table 1**), leading to the final equations for r_r and r_p in **Eq. 6** and **Eq. 7.**

2.6 Parameter estimation and sensitivity analysis

A major factor in dynamic modelling of biological systems is the estimation of model parameters. To estimate the parameters for the current models, a nonlinear least-squares optimization problem was formulated (**Eq. 5**), with the objective of minimizing the least absolute errors (LAE):

$$\mathrm{LAE} = \sum_{\mathrm{i}=1}^{\mathrm{i}=10} \sum_{\mathrm{j}=1}^{\mathrm{j}=130} \left| c(t_j, x_i, y_i) - c_{exp}(t_j, x_i, y_i) \right|$$

Eq. 5

where $c_{exp}(t_j, x_i, y_i)$ is the experimental concentration of oxygen and $c(t_j, x_i, y_i)$ the predicted oxygen concentration from the model for ten chosen points on the sensor foil geometry. Four of the points are located near the center of the photogranule, four points are within its filaments and two points are in the bulk (**Fig. S1**). (x_i, y_i) are the x- and y-coordinates of point *i* and t_j is the acquisition time of image *j*.

The parameter estimation was carried out using the MATLAB function 'fmincon' which allows finding the minimum of a constrained nonlinear multivariable function. The two parameters q_{r0} and q_{p0} were estimated during this minimization problem (**Table 1).**

Table 1 Evaluation of various scenarios relating respiration ($q_r(f)$), photosynthetic activities ($q_p(f)$) and light availability ($I(f)$) to surface-based biomass densities (f). For each scenario, maximum respiration and photosynthesis rates (q_{r0} and q_{p0}) as used in the reaction-diffusion model (Equations 3 and 4) were estimated, using the least absolute errors as criterion from which the mean absolute error (MAE) was computed. Scenario 4 (in bold) was retained for all further analyses.

Model scenarios				**Estimated rates and error**		
#	$q_r(f)$	$q_p(f)$	$I(f)$	q_{r0} (mmol·m^{-3}·s^{-1})	q_{p0} (m^{-1})	**MAE (% air saturation)**
1	$q_{r0} \cdot f$	$q_{p0} \cdot f$	$I_0 \cdot (1-f)$	0.75	25.4	3.7
2	q_{r0}	$q_{p0} \cdot f$	$I_0 \cdot (1-f)$	0.45	16.6	4.4
3	$q_{r0} \cdot f$	q_{p0}	$I_0 \cdot (1-f)$	1.04	26.6	3.8
4	$\boldsymbol{q_{r0}}$	$\boldsymbol{q_{p0}}$	$\boldsymbol{I_0 \cdot (1-f)}$	**0.55**	**17.5**	**3.8**
5	$q_{r0} \cdot f$	$q_{p0} \cdot f$	I_0	0.22	5.6	8.4
6	q_{r0}	$q_{p0} \cdot f$	I_0	0.52	5.6	5.4
7	$q_{r0} \cdot f$	q_{p0}	I_0	4.71	2.6	8.9
8	q_{r0}	q_{p0}	I_0	2.93	33.6	8.7

3 Results

3.1 Spatio-temporal oxygen distribution

The photogranule used in this study and the area analyzed with the VisiSens system are shown in Erreur ! Source du renvoi introuvable.**g**. Area-based biomass density is approximated as grey levels on the image where darker grey level mean higher biomass density. The photogranule contour (**Fig. 3b**) resulted from manual thresholding, best differentiating the spatial domain of the photogranule (grey levels) from the bulk liquid (white). Maps of oxygen concentrations were extracted from images acquired after exciting the oxygen-sensitive film placed underneath the photogranule. Local oxygen concentrations were extracted and plotted over time for points P1-P5 (Erreur ! Source du renvoi introuvable.**f** and Erreur ! Source du renvoi introuvable.**g**). Note that the optode measures oxygen at the interface between the oxygen sensitive sensor foil and the photogranule. Therefore, positions of the points are strictly speaking found at this interface as indicated in Erreur ! Source du renvoi introuvable.**f**. Points P1 and P2 are located under the core area of the photogranule. Here, the initial oxygen concentration starts around 20% oxygen saturation and rapidly decreases to less than 5% during the first dark phase. It then remains stable at this level until the end of the experiment. Points P3 and P4 are located within the filaments. The oxygen concentrations here are initially at 50-60% of the saturation concentration and decrease in the first dark phase to around 5% for P3 and 10% for

P4. Especially at P4, an oscillation of the concentration is then observed with an increase of about 5% during the light phases and a decrease of about 5% during the dark phase. At point P5, located outside the photogranule, the oxygen concentration oscillates in a similar manner as at P3 and P4. The mean value and the amplitude of the oscillations are, however, greater for P5 than for P3 and P4, with values around 60% and 10%, respectively.

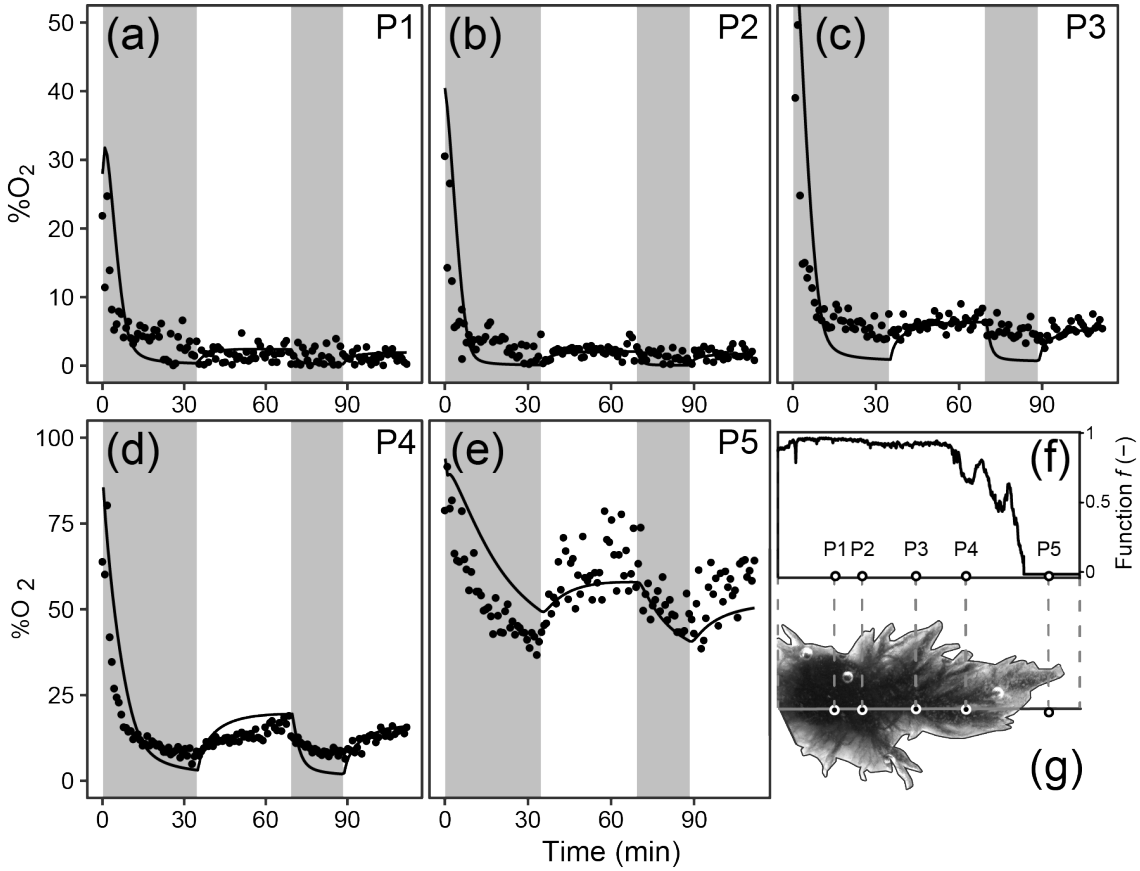

Fig. 4 Oxygen dynamics at five points of interest and their location in the photogranule. (a) – (e) Oxygen concentrations (with respect to the saturation concentration when exposed to air) at points P1 to P5 over time. The points are measured data, solid lines are the model output using scenario 4 (Table 1). The shaded areas indicate the dark and light phases of the experiment. (f) The transformed grey level profile of the transect connecting points P1-P5 in the photogranule, as used for function f in Eq.s 3, 4, and 7 and Table 1. (g) Bird's eye view of the location of points P1 – P5 in the photogranule. Note: This image is a rotated version Fig. 3b.

3.2 2D reaction-diffusion model

With the 2D model, we tested a set of scenarios relating respiration and phototrophic activities to the local biomass densities *f* (**Table 1**). Among the scenarios, we identified the one that best captured the influence of the 3D structure of the photogranule on the dynamics of oxygen concentrations at the surface of the VisiSens sensitive film, evidenced by the best fit between model and experimental data.

The scenarios in **Table 1** include configurations in which (i) both, respiration and phototrophic activities ($q_r(f)$ and $q_p(f)$, respectively), are proportional to local biomass densities (scenarios 1 or 5); (ii) only one of them is proportional local biomass densities (scenarios 2, 3, 6, 7); or (iii) both are independent of local biomass densities (scenarios 4 and 8). Also light intensity *I(f)* was tested as a function of local biomass densities: (i) *I(f)* could be inversely proportional to biomass density, (scenarios 1-4). This corresponds to photosynthetic activity predominantly towards the outside of

the photogranule, where local biomass densities are low and being attenuated towards the center of the photogranule. (ii) Alternatively, *I(f)* was tested to equal I_0 = 61 PAR throughout the photogranule if we assume that the measured photosynthetic activity results from the whole photogranule (scenarios 5-8).

For each scenario of the model, parameters q_{r0} and q_{p0} were optimized to obtain the best fit for ten selected points (P1-P5 and five additional points, see **Fig. S1**). Estimated rates and mean absolute error (MAE) are shown in **Table 1**. Scenarios 1-4 deviate less from the experimental measurements than scenarios 5-8, as indicated by their lower MAE. This is confirmed by a more detailed analysis of the fits in which we analyzed the local behavior at each of the ten selected points (supplementary material **Figs. S2 – S11**). Including a light dependency related to biomass density in the model apparently improves the quality of the model output. Among these scenarios, scenarios 1, 3 and 4 have the lowest MAE and behave similarly at the ten examined points (**Fig. S1**). We thus decided to retain the simplest of the three, scenario 4, for all consequent analyses. Using scenario 4, **Eq. 3** and **Eq. 4** become:

$$r_r = q_{r0} \cdot \frac{C}{C + K}$$

Eq. 6

$$r_p = q_{p0} \cdot I_0 \cdot (1 - f)$$

Eq. 7

The model then allowed us to deconvolute the three processes of respiration, photosynthesis and diffusion from spatially-structured oxygen measurements. We integrated their rates over the total 2D surface delimited by the contour of the photogranule (**Fig. 3b**). The dynamics of surface integrated rates are shown in **Fig. 5**.

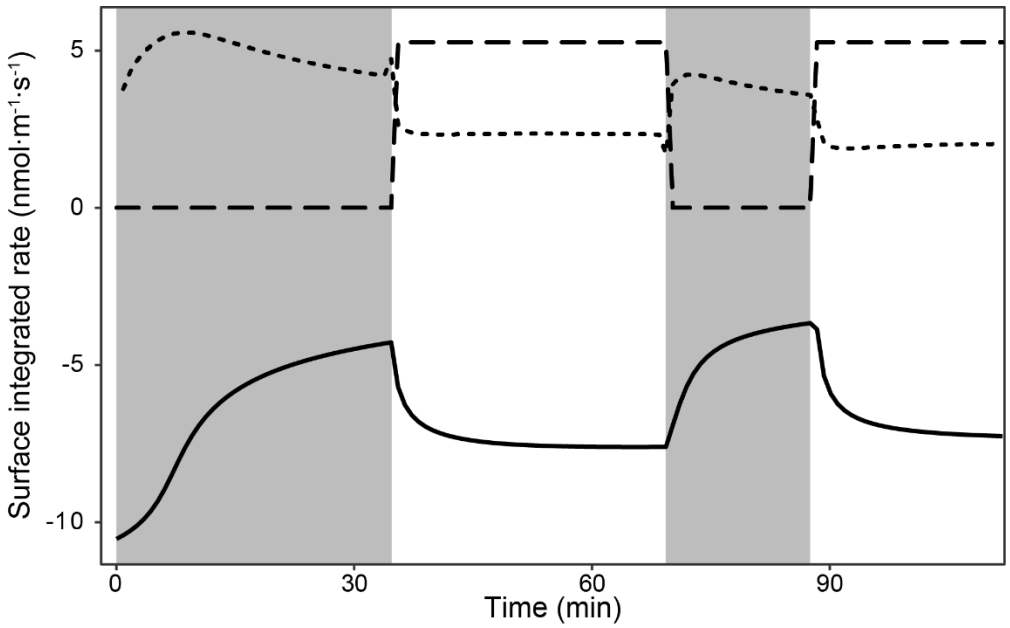

Fig. 5 Surface integrated rates of modeled respiration (solid line), photosynthesis (dashed line) and diffusion (dotted line) over the course of the experiment for the entire photogranule. The surface used for the integration corresponds to the area inside the contour in Fig. 3b. The shaded areas here indicate the dark and light phases of the experiment. O_2 consumption by respiration is expressed as a negative rate while O_2 production by photosynthesis is positive. Diffusion can be either positive when O_2 is imported into the photogranule or could be negative when it is exported.

At the beginning of the two dark phases, the initial respiration was relatively high, as indicated by relatively low negative rates of -10.5 and -7.6 nmol·m^{-1}·s^{-1}. The respiration activity then decreased during the phases and the associated rates reached -4.3 and -3.7 nmol·m^{-1}·s^{-1} during the first and second dark phase, respectively. At the end of the phases, the system was close to steady state and diffusion nearly compensated oxygen consumption by respiration with rates of 4.7 and 3.6 nmol·m^{-1}·s^{-1}. Conversely, respiration rates increased during light phases and reached -7.6 and -7.3 nmol·m^{-1}·s^{-1}. This was associated with a constant photosynthesis rate of 5.3 nmol·m^{-1}·s^{-1}. The oxygen flux towards the photogranule by diffusion was lower during light phases than during dark phases (2.7 et 2.0 nmol·m^{-1}·s^{-1}), but the photogranule remained a net consumer of externally provided oxygen. At the end of each dark or light phase, the system was near steady state. Steady state was reached only during the first light phase that lasted 35 minutes. Globally, for all the phases, a time on the order of 30 minutes is required for the system to reach a steady state.

3.3 Sensitivity analysis

We assessed the uncertainty of parameters q_{r0} and q_{p0} by varying their values around their optima of 0.55 mmol·m^{-1}·s^{-1} and 17.5 m^{-1} (**Table 1**) and computing the resulting MAE (**Fig. 6**). At a MAE of up to 4 %O_2 (i.e., an increase in MAE of about 5% compared to the optimal MAE of scenario 4), the retained couples of (q_{r0}, q_{p0}) fall within the central ellipse in **Fig. 6**. The minimal and maximal values associated with this ellipse are between 0.52 and 0.65 for q_{r0} and between 15.6 and 22.6 for q_{p0}. However, there is a strong positive correlation between q_{r0} and q_{p0}, i.e., when q_{r0} increases, also q_{p0} increases. The uncertainty on the values for q_{r0} and q_{p0} is quite high with a possible relative error of 18% and 29%, respectively, when we compare the optimal couple (0.55 mmol·m^{-3}·s^{-1}, 17.5 m^{-1}) with the extreme acceptable values of (0.65 mmol·m^{-3}· s^{-1}, 22.6 m^{-1}).

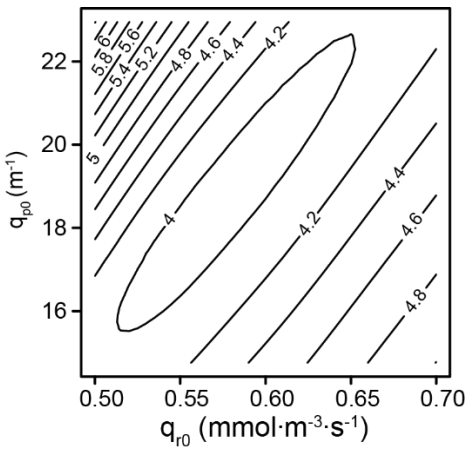

Fig. 6 Contour plot of mean absolute error (MAE in %O2) of the model as function of qr0 and qp0. The minimum is found for q_{r0} = 0.55 mmol·m^{-3}·s^{-1} and q_{p0} = 17.5 m^{-1} as shown in Table 1. The area within the ellipse where MAE = 4 %O_2 corresponds to combinations of q_{r0} and q_{p0} for which MAE ≤ 4 %O_2.

4 Discussion

The coexistence of multiple granule morphologies is common in granular sludge bioreactors. This was reported for phototrophic algal-bacterial biomass under batch or continuous cultivation with synthetic medium (Brehm et al., 2003) or real wastewater (Arcila and Buitrón, 2017) for anammox sequencing batch reactors treating municipal wastewater (Pijuan et al., 2020) or sequencing batch reactors with aerobic granular sludge treating synthetic or real wastewater (Layer et al., 2019; Pronk et al., 2015; Schambeck et al., 2020). In our photobioreactor, we observed the coexistence of a range of morphologies, from filament-covered photogranules to nearly spherical photogranules (**Fig. 1**).

System performance results from the interactions of microorganisms within each granule but also between the populations inhabiting granules of diverse morphologies and sizes (Kuroda et al., 2016; Liu et al., 2020). The different morphologies of biomass are believed to be essential for the proper functioning of the bioreactors (Vannecke et al., 2015). Therefore, breaking down the contributions by morphologic granule population may become necessary for predicting overall reactor performance, especially when the abundance distributions of size and morphology classes may be changing. This could be done by physically separating major populations and quantifying the performance of a more uniform composite sample (Abouhend et al., 2020), or by measuring the activities of individual granules. With data from both approaches, whole reactor performance can be extrapolated using mathematical models. These models do not exist yet but would be preferable over an "average biomass" model as these models would be able to take into consideration temporally non-steady distributions of granule size and morphology.

The microenvironment of individual granules with a clearly defined boundary and a somewhat solid structure is readily accessible using microelectrodes as done for example by Okabe et al (2011) in anammox granules. Using the classic microelectrode approaches, examining the microenvironment of photogranules of filamentous morphology is more challenging because of the ill-defined boundary of the photogranule and its flexible filaments.

We demonstrate here first advances for measuring the activity of filaments in a filamentous photogranule morphology using optodes. In this technology, an oxygen sensitive sensor foil is used to generate an optical signal proportional to the measured oxygen concentration. The resulting images represent a map of oxygen concentrations at the interface with the oxygen sensitive sensor foil. For thin filaments and other labile objects as for example streamers, e.g., points P4 and P5 (Erreur ! Source du renvoi introuvable.**d** and Erreur ! Source du renvoi introuvable. **4e**) the measurement can be assumed to represent the behavior of the biomass. However, for denser regions of photogranules, e.g., at points P1 and P2 (Erreur ! Source du renvoi introuvable.**a** and Erreur ! Source du renvoi introuvable.**b**), the biomass in contact with the oxygen sensitive sensor foil may not be photosynthetically active. Indeed, as light may not penetrate all the way through the denser regions, no photosynthetically active radiation reaches the oxygen sensitive sensor foil. Consequently, the potential local photosynthetic activity cannot be directly measured.

To an extent, mathematical modeling circumvents this limitation. Using a reaction-diffusion model, we were able to deconvolute the images of oxygen concentrations acquired with the optode into photosynthetic oxygen production, heterotrophic respiration, and diffusive transport from the bulk liquid into the photogranules (**Fig. 5**). This knowledge cannot be easily deduced from the interpretation of the raw experimental data.

A remarkably simple model structure containing two parameters was able to capture the essential dynamics of photogranule activities (Erreur ! Source du renvoi introuvable.). We tested various scenarios of spatial distributions of phototrophic and heterotrophic biomass and two illumination types (non-obstructed and attenuated light) (**Table 1**). The best fits of experimental data with the model was achieved in scenarios where light was attenuated following the function *f* (Erreur ! Source du renvoi introuvable.**f**). None of the non-obstructed light scenarios (**Table 1**, scenarios 5-8), including all tested biomass distributions, reached similarly well-fitting results. Three biomass distributions (scenarios 1, 3 and 4) were similar in their fits but we retained scenario 4 as the most parsimonious model. It assumes a homogenous distribution of heterotrophic and phototrophic biomass at all points within the photogranule domain. In scenario 4, light is available for photosynthesis inversely proportional to the surface-based biomass density (function *f*). It appears that the attenuation of light as a function of the surface-based biomass density was more important for the fit of the model than the biomass distributions. Our results indicate that a focus of

future research should be the penetration of light into phototrophic biomass as this phenomenon seems a more sensitive factor for activity than the distribution of biomass. Our result confirms what Abouhend et al (2020) found when relating specific oxygen production rates to photogranule size. The optimal size range of photogranules were found to have diameters between 0.5 to 1 mm, corresponding to photogranules with a homogeneous distribution of phototrophs and diameter allowing light penetration throughout the photogranule (Abouhend et al., 2020).

Under the current experimental conditions, even under illumination, the oxygen supply by diffusion is not negligible, especially considering that respiration was limited to residual organic matter contained in the photogranule. With a greater pool of readily available organic matter, as for example contained in wastewater, respiration would be expected to be higher, requiring a higher oxygen supply. Considering our measurements, this higher contribution could not be provided through photosynthesis with an average irradiation of 61 PAR. Using our model, we calculated that an illumination of at least 120 PAR would satisfy oxygen requirements beyond endogenous respiration, enabling the degradation of externally supplied organic matter. Abouhend et al (2020) observed the degradation of externally supplied organic matter at 150 PAR. Even though our calculations and a comparison with literature values may indicate possible light requirements for wastewater treatment using photogranules, this consideration should be taken with care, as the values were obtained using very different experimental procedures and systems. The minimum light requirements may be lower as we assume as our experimental procedure may underestimate or hinder oxygen production.

One identified reason for underestimating actual oxygen production is linked to the required exposure time of 20 s for image acquisition of the optode system. During acquisition, external photosynthetically active radiation needed to be stopped, while the light-independent oxygen consumption continued. The resulting images thus represent an integral over 20 s of oxygen consumption. Due to the possible non-linearity of the responses, we refrained from estimating a consumption term to compensate this loss. A further drawback of the long acquisition time, though less relevant in our situation, is the detection of processes with shorter characteristic times than needed for acquisition, e.g., oxygen production in moving filaments.

Our 2D model, by definition, only considers a projection of a three-dimensional photogranule onto a two-dimensional surface. This projection, however, is not a true average signal over the depth of biomass, but in a sense a weighted average, giving most weight to the interface with the oxygen sensitive sensor foil. The global photosynthetic activity may thus be underestimated. Indeed, photosynthetic activity at the light-exposed surface of the photogranule, e.g., above points P1 and P2, may not be detectable at the film interface as all oxygen will have been consumed in upper parts of the photogranule. The effect of the projection may explain the discrepancy between model and experimental data at P3 (Erreur ! Source du renvoi introuvable.**c**). Here, the model underestimates the experimentally measured oxygen concentrations possibly because diffusion from the bulk phase overlaying the photogranule may supply oxygen that is unaccounted for in the 2D model. It may also happen that available surface for photosynthesis, e.g., filaments protruding into the bulk phase in the dynamic flow field during reactor operation, may collapse during the hydrodynamically static experiment and thus reduce the available area for photosynthetic activity.

Knowing that the photogranules from our reactor are in principle able to provide sufficient quantities of oxygen for the degradation of a synthetic wastewater (unpublished data), we assume that a reduction in photosynthetic activity must have happened during our experiments. Otherwise we would have noticed a gradual aeration of the bulk phase, eventually leading to supersaturation with respect to atmospheric oxygen as regularly observed in the lab scale reactors. Instead, at distant points from the photogranule, a decrease in oxygen concentrations was detected (e.g., P6 in **Fig. S1**).

This indicates that oxygen consumption due to respiration in the photogranule was always higher than oxygen production due to photosynthesis.

Despite the experimental limitations of the optode system for the activity measurement of filamentous photogranules, this kind of technology coupled to mathematical modeling is able to provide essential data on the activity of filaments, i.e., their activity per surface as done here (Erreur ! Source du renvoi introuvable. and **Fig. 5**). This information is useful for optimizing a bioprocess using photogranules. We were able to demonstrate that in the filaments the characteristic response time of changes in the oxygen dynamics after phases of darkness is on the order of seconds. This implies that the exposure to varying light on the trajectory of a photogranule in a photobioreactor may influence the activity of photogranules, even reversing oxygen gradients. The response of oxygen concentrations in filaments is also linked to the heterotrophic respiration. Filaments therefore do not only offer a surface for oxygen production, but at the same time can be a preferential location for nitrogen and carbon conversion. This rapid shifts of oxic and anoxic periods in a photogranule floating in the photobioreactor may promote shifts in nitrification and denitrification. This is of particular interest for the application of photogranules in the context of wastewater treatment.

5 Conclusions

Our ultimate goal is mathematical description of a photogranular system containing all morphologic populations of photogranules. This work provides a first modeling approach for heterogeneous photogranule morphologies found in filamentous photogranules. Obtaining a unified vision of the activity of this morphotype of photogranules, including all regions within the photogranules, remains to be developed. The use of optodes alone as done in this study needs to be complemented, e.g., by classic microelectrode work, to characterize the denser regions of filamentous photogranule.

Acknowledgements

We are grateful to Philippe Sousbie for assisting in reactor operation during this research, and to Cristian Picioreanu (TU Delft, The Netherlands) for his advice in modeling. This work was financed through the French “Agence Nationale de la Recherche” grant ANR-16-CE04-0001-01 (“PSST: Photogranules shake sewage treatment up”), the INRAE division MICA and the University of Montpellier for a travel grant through the Gaïa doctorate school. We are grateful having received the VisiSens system free of charge by PreSens, Regensburg, Germany.

Declaration of interest

We wish to draw the attention of the Editor to a fact which may be considered as potential conflict of interest: PreSens – Precision Sensing GmbH in D-93053 Regensburg, Germany, graciously provided the VisiSens system free of charge for testing purposes. PreSens was neither involved in the design and conduct of the experiments and nor the analysis of the results. PreSens did not in any way influence the evaluation of the VisiSens system, nor was PreSens involved in the writing of the manuscript. We are therefore confident that our evaluation of the system is free of a conflict of interest.

References

1. Abouhend, A.S., McNair, A., Kuo-Dahab, W.C., Watt, C., Butler, C.S., Milferstedt, K., Hamelin, J., Seo, J., Gikonyo, G.J., El-Moselhy, K.M., Park, C., 2018. The oxygenic photogranule process for aeration-free wastewater treatment. Environ. Sci. Technol. 52, 3503–3511.

https://doi.org/10.1021/acs.est.8b00403
4 Abouhend, A.S., Milferstedt, K., Hamelin, J., Ansari, A.A., Butler, C., Carbajal-González, B.I., Park, C., 2020. Growth progression of oxygenic photogranules and its impact on bioactivity for aeration-free wastewater treatment. Environ. Sci. Technol. 54, 486–496. https://doi.org/10.1021/acs.est.9b04745
5 Ansari, A.A., Abouhend, A.S., Park, C., 2019. Effects of seeding density on photogranulation and the start-up of the oxygenic photogranule process for aeration-free wastewater treatment. Algal Res. 40, 101495. https://doi.org/10.1016/j.algal.2019.101495
6 Arcila, J.S., Buitrón, G., 2017. Influence of solar irradiance levels on the formation of microalgae-bacteria aggregates for municipal wastewater treatment. Algal Res. 27, 190–197. https://doi.org/10.1016/j.algal.2017.09.011
7 Brehm, U., Krumbein, W.E., Palińska, K. a, 2003. Microbial spheres: a novel cyanobacterial–diatom symbiosis. Naturwissenschaften 90, 136–140. https://doi.org/10.1007/s00114-003-0403-x
8 Faizi, M., Steuer, R., 2019. Optimal proteome allocation strategies for phototrophic growth in a light - limited chemostat. Microb. Cell Fact. 1–18. https://doi.org/10.1186/s12934-019-1209-7
9 Glud, R.N., Tengberg, A., Kühl, M., Hall, P.O.J., Klimant, I., 2001. An in situ instrument for planar O2 optode measurements at benthic interfaces. Limnol. Oceanogr. 46, 2073–2080. https://doi.org/10.4319/lo.2001.46.8.2073
10 Horn, H., Hempel, D.C., 1997. Growth and decay in an auto-/heterotrophic biofilm. Water Res. 31, 2243–2252. https://doi.org/10.1016/S0043-1354(97)00081-X
11 Koop-Jakobsen, K., Mueller, P., Meier, R.J., Liebsch, G., Jensen, K., 2018. Plant-sediment interactions in salt marshes – An optode imaging study of O2, pH, and CO2 gradients in the rhizosphere. Front. Plant Sci. 9, 1–11. https://doi.org/10.3389/fpls.2018.00541
12 Kuroda, K., Nobu, M.K., Mei, R., Narihiro, T., Bocher, B.T.W., Yamaguchi, T., Liu, W.-T., 2016. A single-granule-level approach reveals ecological heterogeneity in an upflow anaerobic sludge blanket reactor. PLoS One 11, e0167788. https://doi.org/10.1371/journal.pone.0167788
13 Larsen, M., Borisov, S.M., Grunwald, B., Klimant, I., Glud, R.N., 2011. A simple and inexpensive high resolution color ratiometric planar optode imaging approach: Application to oxygen and pH sensing. Limnol. Oceanogr. Methods 9, 348–360. https://doi.org/10.4319/lom.2011.9.348
14 Layer, M., Adler, A., Reynaert, E., Hernandez, A., Pagni, M., Morgenroth, E., Holliger, C., Derlon, N., 2019. Organic substrate diffusibility governs microbial community composition, nutrient removal performance and kinetics of granulation of aerobic granular sludge. Water Res. X 4, 100033. https://doi.org/10.1016/j.wroa.2019.100033
15 Liu, Y., Ngo, H.H., Guo, W., Wang, D., Peng, L., Wei, W., Ni, B.-J., 2020. Impact of coexistence of sludge flocs on nitrous oxide production in a granule-based nitrification system: A model-based evaluation. Water Res. 170, 115312. https://doi.org/https://doi.org/10.1016/j.watres.2019.115312
16 Longo, S., d'Antoni, B.M., Bongards, M., Chaparro, A., Cronrath, A., Fatone, F., Lema, J.M., Mauricio-Iglesias, M., Soares, A., Hospido, A., 2016. Monitoring and diagnosis of energy consumption in wastewater treatment plants. A state of the art and proposals for improvement. Appl. Energy 179, 1251–1268. https://doi.org/10.1016/j.apenergy.2016.07.043
17 Mancuso, S., Papeschi, G., Marras, A.M., 2000. A polarographic, oxygen-selective, vibrating-microelectrode system for the spatial and temporal characterisation of transmembrane oxygen fluxes in plants. Planta 211, 384–389. https://doi.org/10.1007/s004250000296
18 Milferstedt, K., Hamelin, J., Park, C., Jung, J., Hwang, Y., Cho, S.K., Jung, K.W., Kim, D.H., 2017a. Biogranules applied in environmental engineering. Int. J. Hydrogen Energy 42, 27801–27811.

https://doi.org/10.1016/j.ijhydene.2017.07.176

19 Milferstedt, K., Kuo-Dahab, W.C., Butler, C.S., Hamelin, J., Abouhend, A.S., Stauch-White, K., McNair, A., Watt, C., Carbajal-González, B.I., Dolan, S., Park, C., 2017b. The importance of filamentous cyanobacteria in the development of oxygenic photogranules. Sci. Rep. 7, 1–15. https://doi.org/10.1038/s41598-017-16614-9

20 Nopens, I., Capalozza, C., Vanrolleghem, P.A., 2001. Stability analysis of a synthetic municipal wastewater. Tech. Rep. Dept. Appl. Math. Biometrics Process Control. Univ, Gent.

21 Okabe, S., Oshiki, M., Takahashi, Y., Satoh, H., 2011. N2O emission from a partial nitrification–anammox process and identification of a key biological process of N2O emission from anammox granules. Water Res. 45, 6461–6470. https://doi.org/https://doi.org/10.1016/j.watres.2011.09.040

22 Pijuan, M., Ribera-Guardia, A., Balcázar, J.L., Micó, M.M., de la Torre, T., 2020. Effect of COD on mainstream anammox: Evaluation of process performance, granule morphology and nitrous oxide production. Sci. Total Environ. 712, 136372. https://doi.org/https://doi.org/10.1016/j.scitotenv.2019.136372

23 Pischedda, L., Poggiale, J.C., Cuny, P., Gilbert, F., 2008. Imaging oxygen distribution in marine sediments. The importance of bioturbation and sediment heterogeneity. Acta Biotheor. 56, 123–135. https://doi.org/10.1007/s10441-008-9033-1

24 Pronk, M., Abbas, B., Al-zuhairy, S.H.K., Kraan, R., Kleerebezem, R., van Loosdrecht, M.C.M., 2015. Effect and behaviour of different substrates in relation to the formation of aerobic granular sludge. Appl. Microbiol. Biotechnol. 99, 5257–5268. https://doi.org/10.1007/s00253-014-6358-3

25 Quaranta, M., Borisov, S.M., Klimant, I., 2012. Indicators for optical oxygen sensors. Bioanal. Rev. 4, 115–157. https://doi.org/10.1007/s12566-012-0032-y

26 Revsbech, N.P., Jørgensen, B.B., 1986. Microelectrodes: their use in microbial ecology, in: Advances in Microbial Ecology. pp. 293–352. https://doi.org/10.1007/978-1-4757-0611-6_7

27 Rubol, S., Freixa, A., Sanchez-Vila, X., Romaní, A.M., 2018. Linking biofilm spatial structure to real-time microscopic oxygen decay imaging. Biofouling 34, 200–211. https://doi.org/10.1080/08927014.2017.1423474

28 Schambeck, C.M., Magnus, B.S., de Souza, L.C.R., Leite, W.R.M., Derlon, N., Guimarães, L.B., da Costa, R.H.R., 2020. Biopolymers recovery: dynamics and characterization of alginate-like exopolymers in an aerobic granular sludge system treating municipal wastewater without sludge inoculum. J. Environ. Manage. 263, 110394. https://doi.org/https://doi.org/10.1016/j.jenvman.2020.110394

29 Schneider, C.A., Rasband, W.S., Eliceiri, K.W., 2012. NIH Image to ImageJ: 25 years of image analysis. Nat. Methods 9, 671–675. https://doi.org/10.1038/nmeth.2089

30 Shoener, B.D., Bradley, I.M., Cusick, R.D., Guest, J.S., 2014. Energy positive domestic wastewater treatment: The roles of anaerobic and phototrophic technologies. Environ. Sci. Process. Impacts 16, 1204–1222. https://doi.org/10.1039/c3em00711a

31 Staal, M., Te Lintel Hekkert, S., Herman, P., Stal, L.J., 2002. Comparison of models describing light dependence of N2 fixation in heterocystous cyanobacteria. Appl. Environ. Microbiol. 68, 4679–4683. https://doi.org/10.1128/AEM.68.9.4679-4683.2002

32 Stauch-White, K., Srinivasan, V.N., Camilla Kuo-Dahab, W., Park, C., Butler, C.S., 2017. The role of inorganic nitrogen in successful formation of granular biofilms for wastewater treatment that support cyanobacteria and bacteria. AMB Express 7, 146. https://doi.org/10.1186/s13568-017-0444-8

33 Trebuch, L.M., Oyserman, B.O., Janssen, M., Wijffels, R.H., Vet, L.E.M.M., Fernandes, T. V., 2020. Impact of hydraulic retention time on community assembly and function of photogranules for

wastewater treatment. Water Res. 173, 115506. https://doi.org/10.1016/j.watres.2020.115506

34 Tschiersch, H., Liebsch, G., Borisjuk, L., Stangelmayer, A., Rolletschek, H., 2012. An imaging method for oxygen distribution, respiration and photosynthesis at a microscopic level of resolution. New Phytol. 196, 926–36. https://doi.org/10.1111/j.1469-8137.2012.04295.x

35 Vannecke, T.P.W., Wells, G., Hubaux, N., Morgenroth, E., Volcke, E.I.P., 2015. Considering microbial and aggregate heterogeneity in biofilm reactor models: How far do we need to go? 1692–1699. https://doi.org/10.2166/wst.2015.389

36 Wenzhöfer, F., Glud, R.N., 2004. Small-scale spatial and temporal variability in coastal benthic O2dynamics: Effects of fauna activity. Limnol. Oceanogr. 49, 1471–1481. https://doi.org/10.4319/lo.2004.49.5.1471

37 Wolf, G., Picioreanu, C., Van Loosdrecht, M.C.M., 2007. Kinetic modeling of phototrophic biofilms: The PHOBIA model. Biotechnol. Bioeng. 97, 1064–1079. https://doi.org/10.1002/bit.21306

Supplementary materials

Mapping the biological activities of filamentous oxygenic photogranules

Hicham Ouazaite, Kim Milferstedt, Jérôme Hamelin, Elie Desmond-Le Quéméner*

INRAE, Univ Montpellier, LBE, 102 Avenue des Etangs, 11100 Narbonne, France
*corresponding author: elie.lequemener@inrae.fr

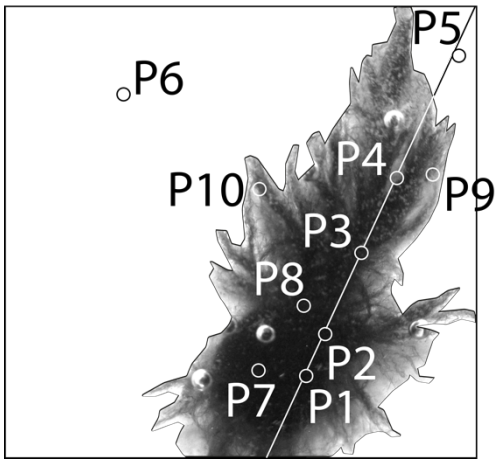

Figure S1: OPG stereomicroscopic image and location of points P1 – P10 used for model calibration. P1, P2, P7 and P8 are located near the center of the photogranule. P3, P4, P9 and P10 are within its filaments. P5 and P6 are in the bulk.

Figures S2 – S11 show the details of the best fits of models for points P1 – P10 associated with scenarios 1 – 8 (see Table 1 in the main text).

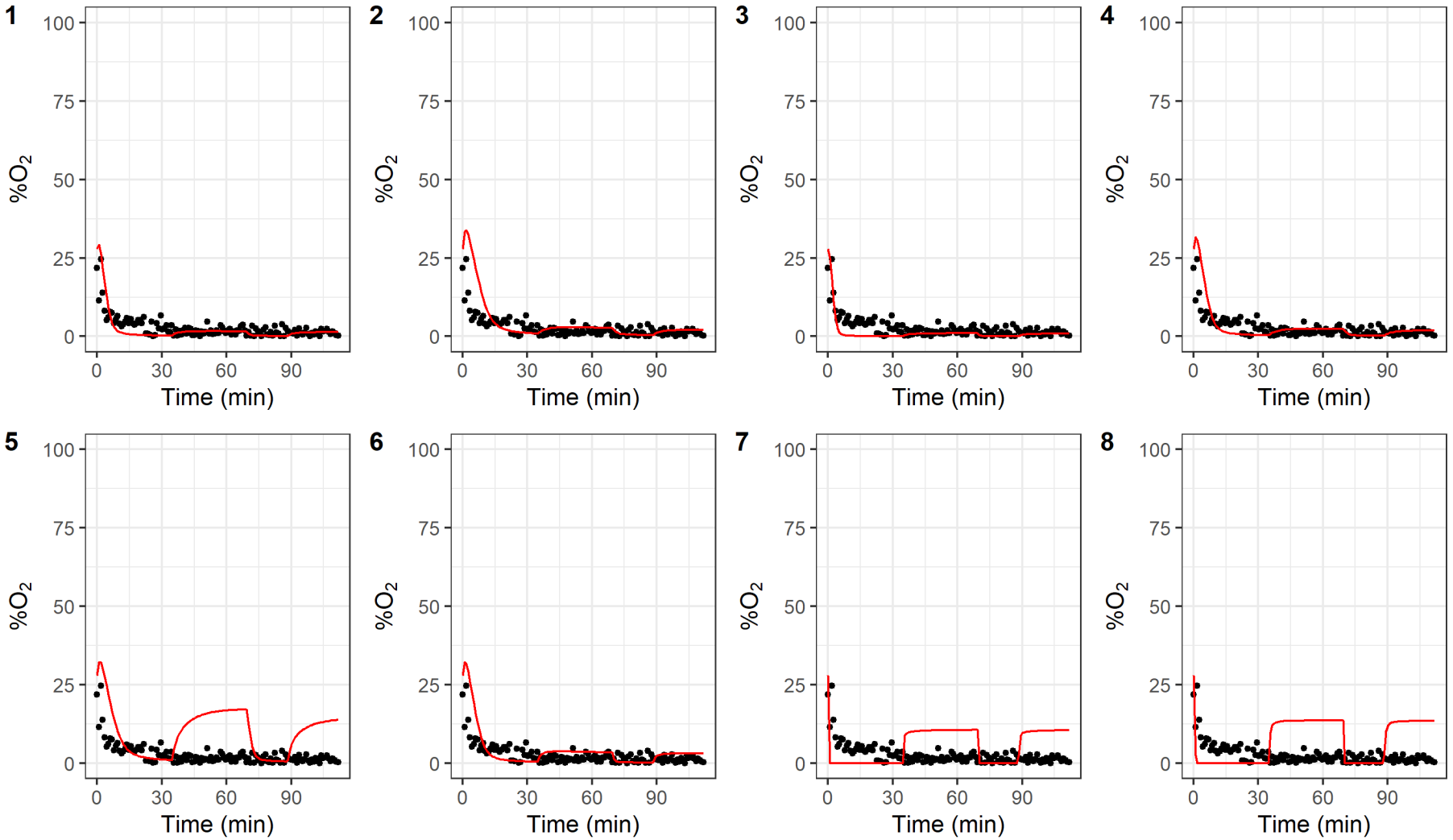

Figure S2: Oxygen saturation (with respect to air) at point **P1** over time. The points are measured data, red solid lines are the model output. Panels 1 - 8 correspond to scenarios 1 - 8 respectively.

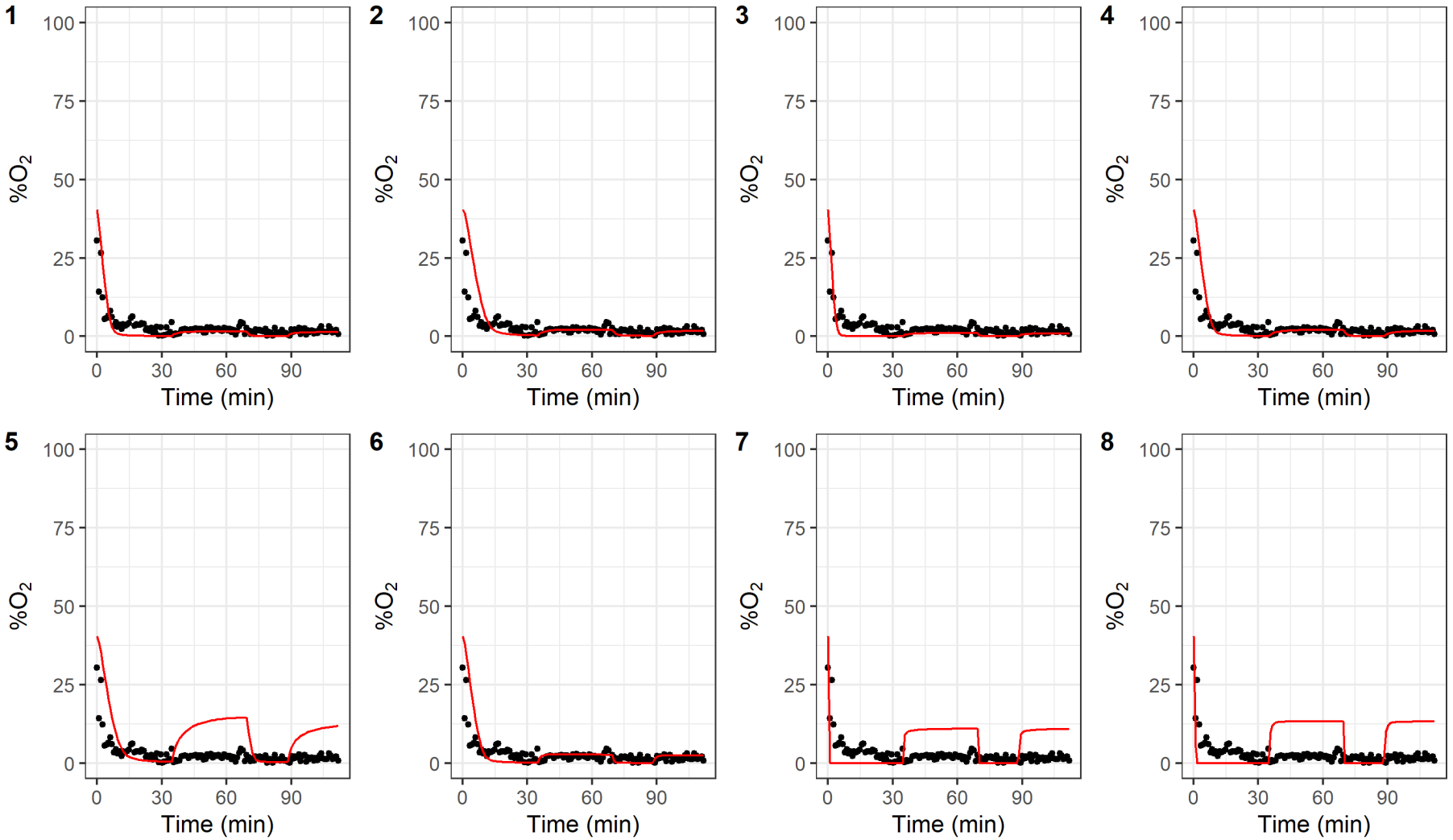

Figure S3: Oxygen saturation (with respect to air) at point **P2** over time. The points are measured data, red solid lines are the model output. Panels 1 - 8 correspond to scenarios 1 - 8 respectively.

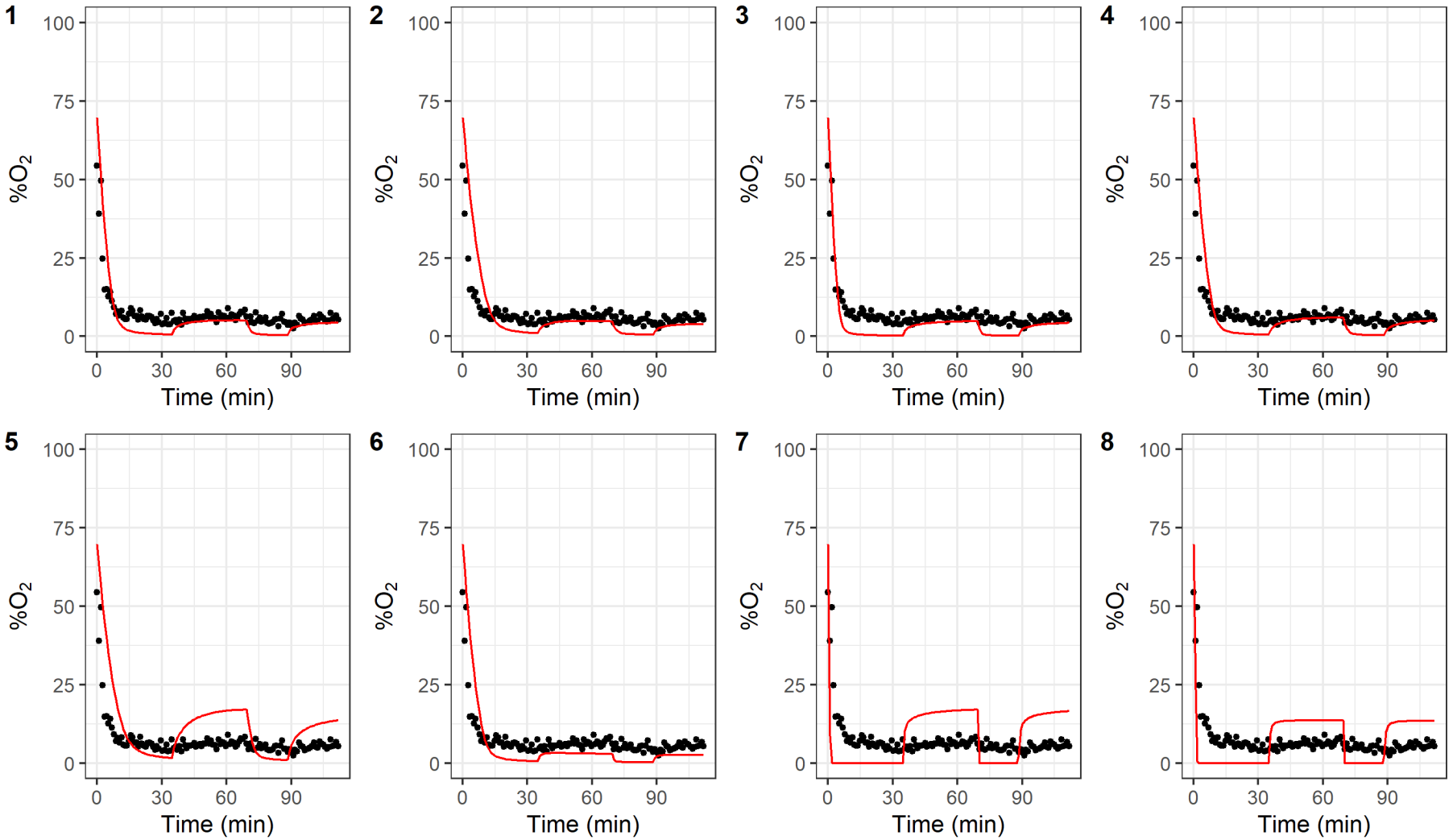

Figure S4: Oxygen saturation (with respect to air) at point **P3** over time. The points are measured data, red solid lines are the model output. Panels 1 - 8 correspond to scenarios 1 - 8 respectively.

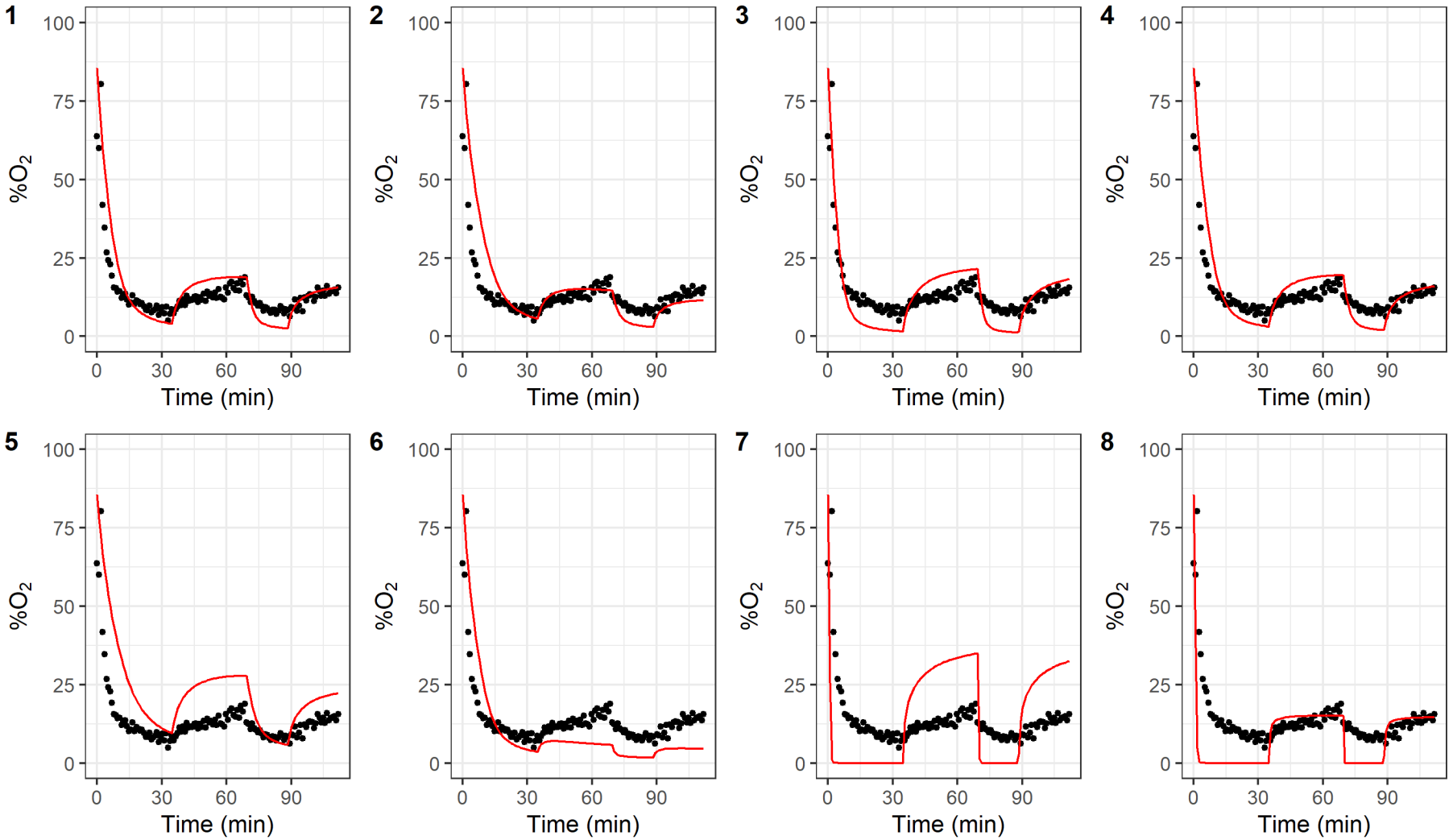

Figure S5: Oxygen saturation (with respect to air) at point **P4** over time. The points are measured data, red solid lines are the model output. Panels 1 - 8 correspond to scenarios 1 - 8 respectively.

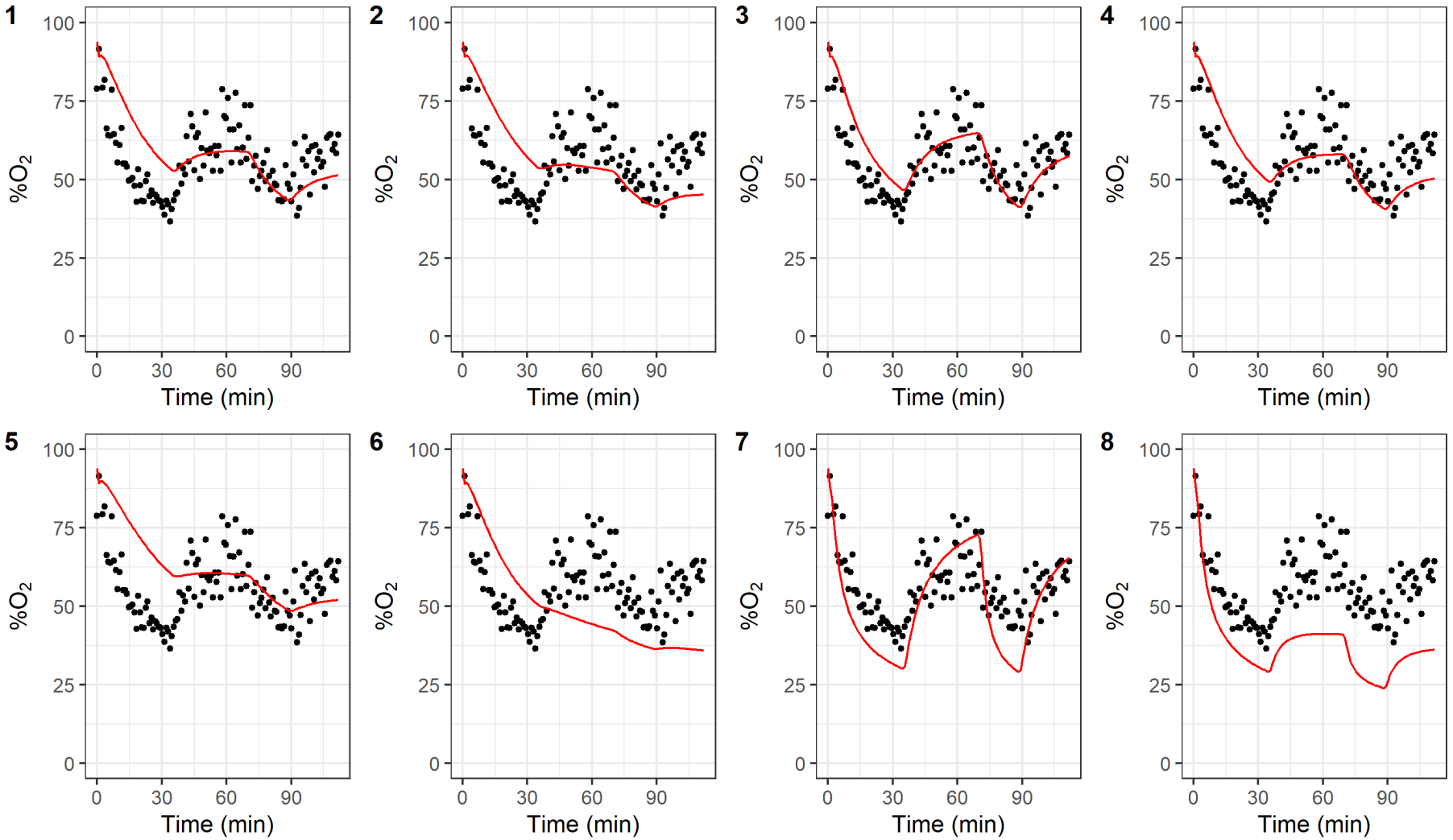

Figure S6: Oxygen saturation (with respect to air) at point **P5** over time. The points are measured data, red solid lines are the model output. Panels 1 - 8 correspond to scenarios 1 - 8 respectively.

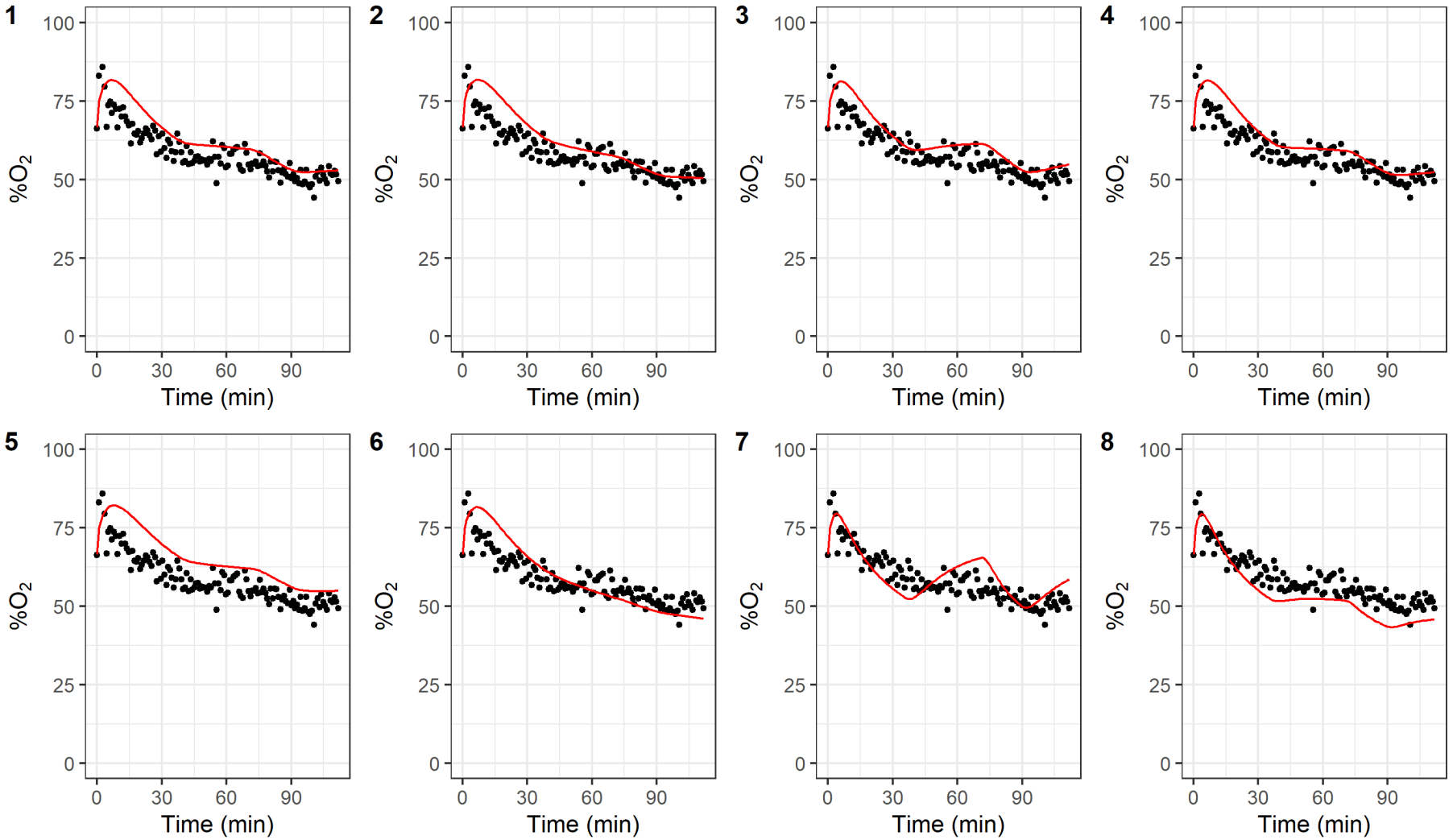

Figure S7: Oxygen saturation (with respect to air) at point **P6** over time. The points are measured data, red solid lines are the model output. Panels 1 - 8 correspond to scenarios 1 - 8 respectively.

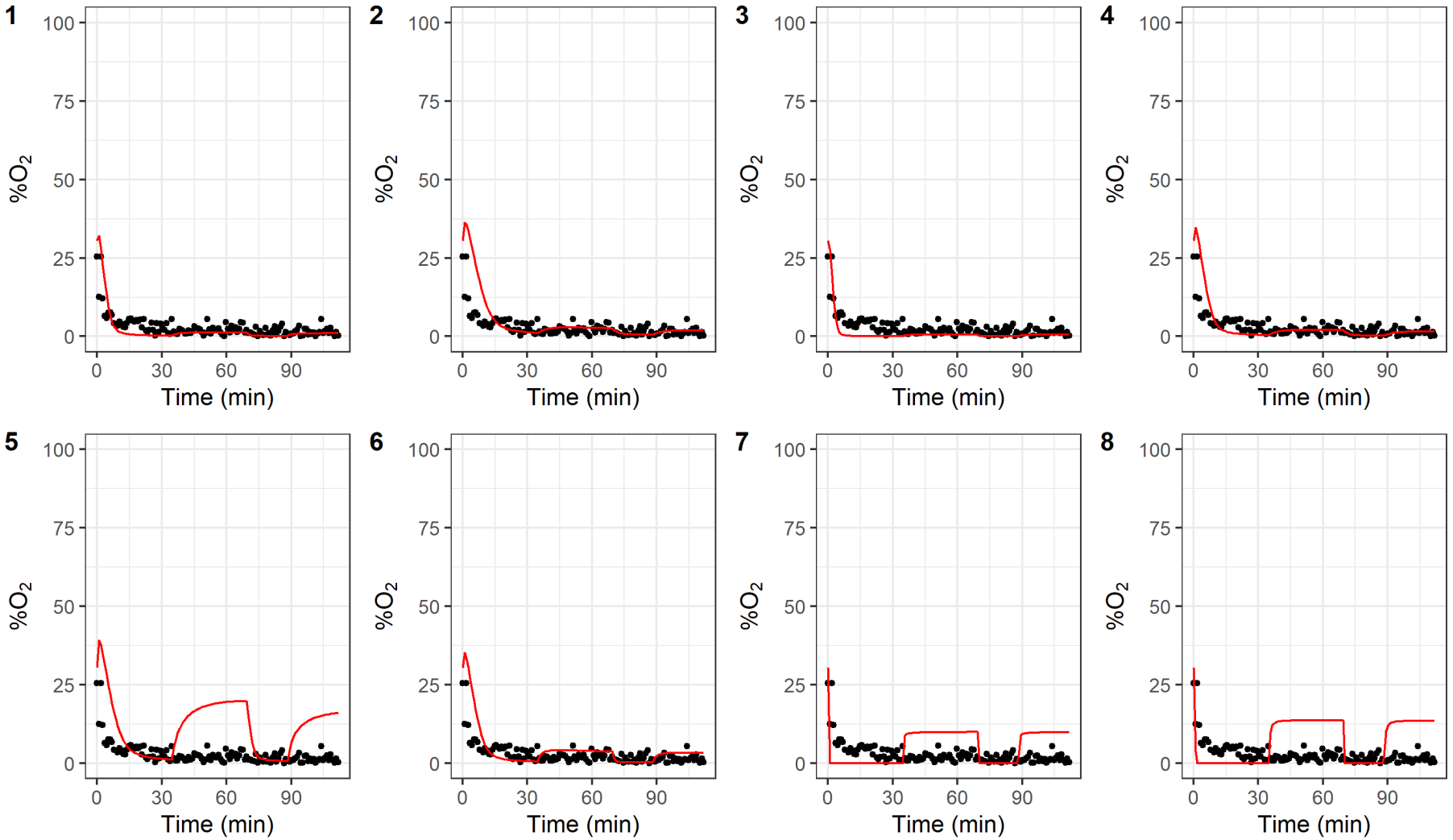

Figure S8: Oxygen saturation (with respect to air) at point **P7** over time. The points are measured data, red solid lines are the model output. Panels 1 - 8 correspond to scenarios 1 - 8 respectively.

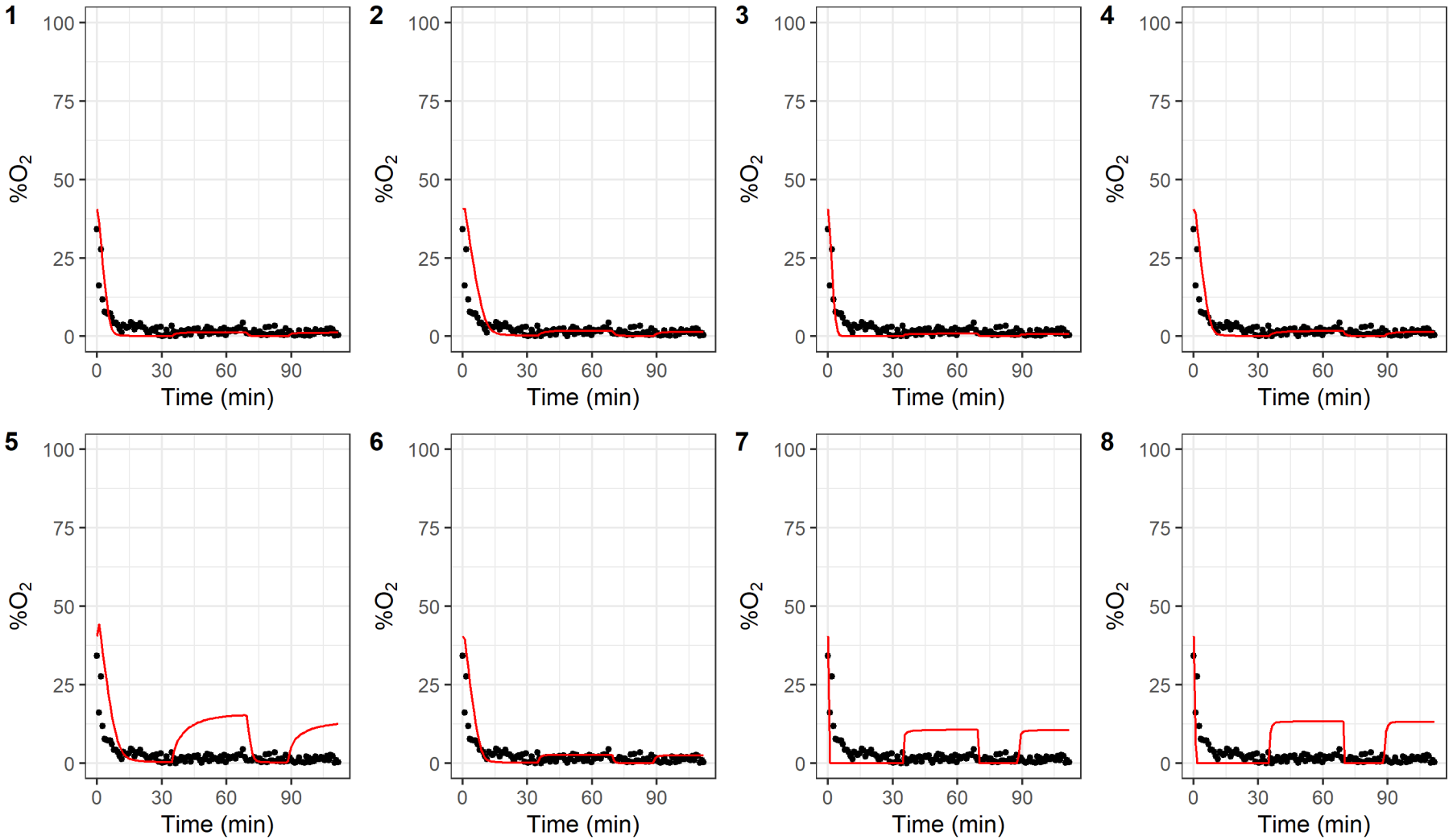

Figure S9: Oxygen saturation (with respect to air) at point **P8** over time. The points are measured data, red solid lines are the model output. Panels 1 - 8 correspond to scenarios 1 - 8 respectively.

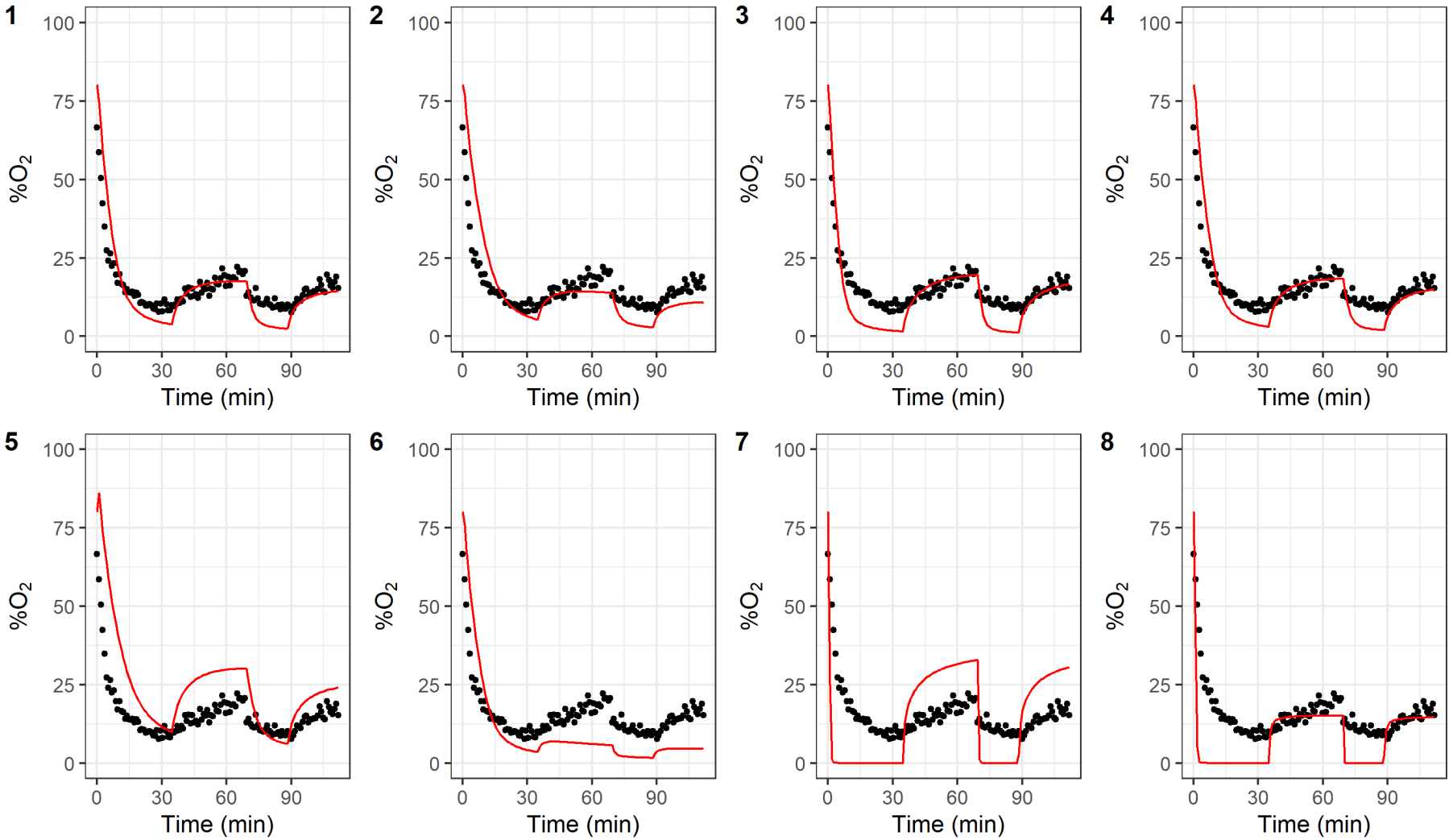

Figure S10: Oxygen saturation (with respect to air) at point **P9** over time. The points are measured data, red solid lines are the model output. Panels 1 - 8 correspond to scenarios 1 - 8 respectively.

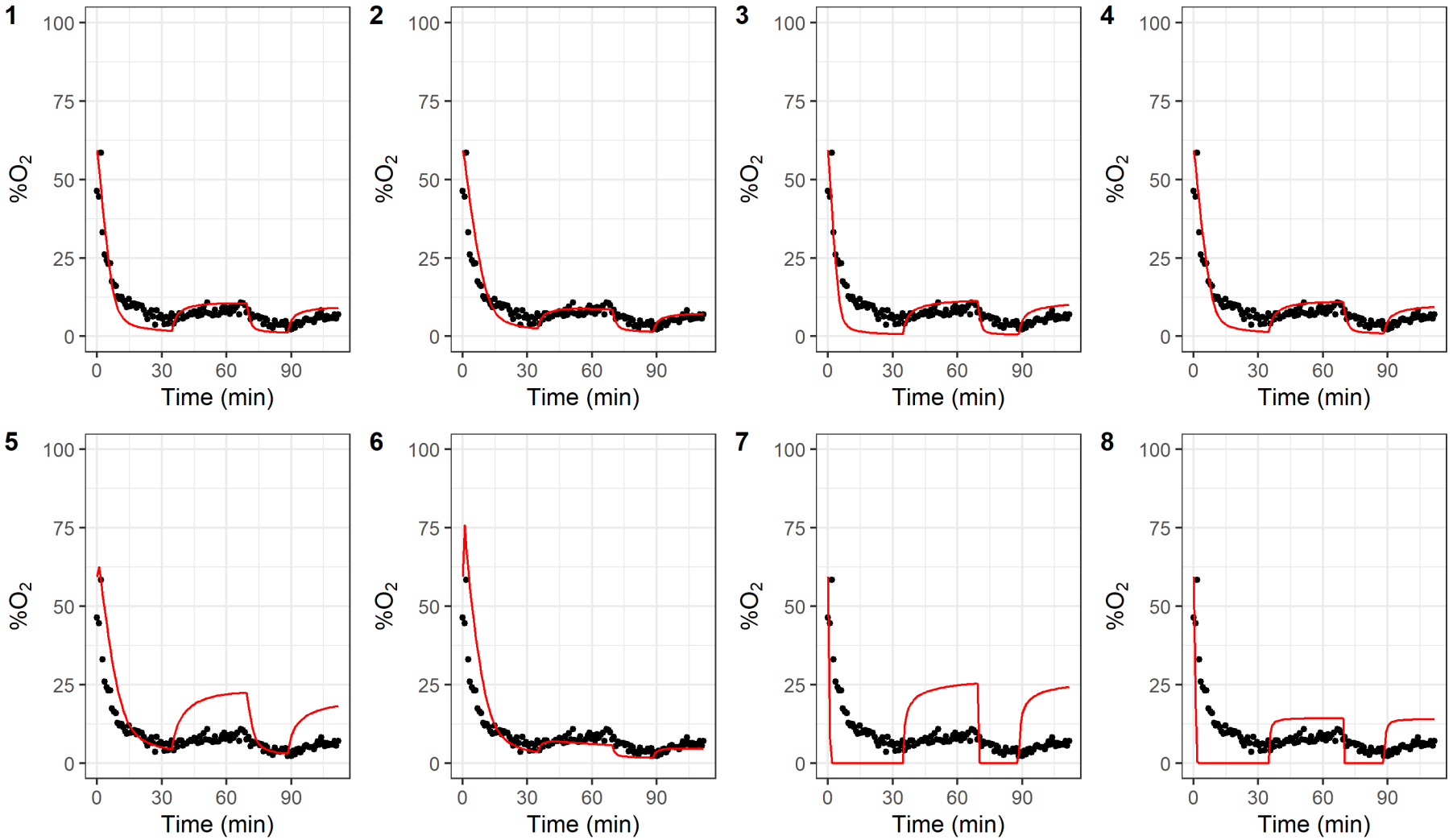

Figure S11: Oxygen saturation (with respect to air) at point **P10** over time. The points are measured data, red solid lines are the model output. Panels 1 - 8 correspond to scenarios 1 - 8 respectively.